The Astrophysical Journal, 947:14 (17pp), 2023 April 10 https://doi.org/10.3847/1538-4357/acb6f2

Gravitational Lensing of Acoustic Charged Black Holes

Niyaz Uddin Molla and Ujjal Debnath
Department of Mathematics, Indian Institute of Engineering Science and Technology, Shibpur, Howrah-711103, India; niyazuddin182@gmail.com, ujjaldebnath@gmail.com
Received 2022 December 3; revised 2023 January 26; accepted 2023 January 27; published 2023 April 12

Abstract

We study the gravitational lensing of acoustic charged black holes in strong and weak field limit approximations. For this purpose, we first numerically obtain the deflection limit coefficients and deflection angle in the strong field limit. We observe that the strong deflection angle α_D increases with increasing magnitude of the charged parameter Q and that the strong deflection angle α_D of an acoustic charged black hole with tuning parameter $\xi = 4$ is greater than that of a standard Reissner–Nordström black hole ($\xi = 0$). We also study the astrophysical consequences via strong gravitational lensing by taking the example of various supermassive black holes in the center of several galaxies and observe that the acoustic charged black hole could be quantitatively distinguished from standard Reissner–Nordström ($\xi = 0$) and standard Schwarzschild ($\xi = 0$, $Q = 0$) black holes. Furthermore, by using the Gauss–Bonnet theorem, we derive the weak deflection angle in the background of an acoustic charged black hole in the curved spacetime. We find that, for fixed values of the charged parameter Q and the tuning parameter ($\xi = 0$ *or* 4), the weak deflection angle σ_D decreases with the impact parameter b. We also observe that the weak deflection angle σ_D decreases with increasing magnitude of the charged parameter Q for a fixed value of the tuning parameter ($\xi = 0$ *or* 4). Our results suggest that the observational test for an acoustic charged black hole is indeed feasible, and it is generalized to the cases of acoustic Schwarzschild ($Q = 0$), standard Reissner–Nordström ($\xi = 0$), and standard Schwarzschild ($\xi = 0, Q = 0$) black holes.

Unified Astronomy Thesaurus concepts: Weak gravitational lensing (1797); Strong gravitational lensing (1643); Gravitational lensing (670)

1. Introduction

One of the most powerful astrophysical tools of general relativity (GR) is gravitational lensing, which is the deflection of a light ray by a gravitational field, and the object causing the deflection is known as a gravitational lens. It provides a useful way to test the fundamental theory of gravity (Will 2015), detect dark matter and dark energy (Kaiser & Squires 1993; Wittman et al. 2000; Massey et al. 2010; Cao et al. 2012; Vanderveld et al. 2012; He & Zhang 2017; Huterer & Shafer 2018; Jung & Shin 2019), measure the masses of clusters of galaxies (Meneghetti et al. 2013; Brouwer et al. 2018; Bellagamba et al. 2019), investigate gravitational waves (Wang et al. 1996; Bisnovatyi-Kogan & Tsupko 2008), etc. As a result, the theory of gravitational lensing can be divided into two regimes. The former case is when the radial distance of a photon is much greater than the radius of the gravitational lens, and the deflection of the light ray becomes small. In this case, two slightly distorted images appear on both sides of the lens. The latter case is when the photon winds around the lens many times before reaching the receiver, known as strong gravitational lensing. In this case, an infinite series of highly magnified images appear on both sides of the lens. The idea of gravitational lensing was first developed in the weak field regime (Refsdal 1964a, 1964b; Schneider et al. 1992; Petters et al. 2001) and then was widely applied in the strong field regime (Darwin 1959; Bozza et al. 2001, 2005; Claudel et al. 2001; Virbhadra & Ellis 2002). Gravitational lensing by compact objects (e.g., black holes (BHs), stars) in the weak and strong field regimes has been studied analytically as well as numerically (Ohanian 1987; Gueth & Guilloteau 1999; Sereno 2003, 2004; Sarkar & Bhadra 2006; Virbhadra & Keeton 2008; Cardoso et al. 2009; Chen & Jing 2009; Hod 2009; Stefanov et al. 2010; Javed et al. 2019b; Kumar et al. 2019, 2020c, 2020a; Shaikh et al. 2019; Islam et al. 2020). The physical observables for the strong lensing effect have been studied by some authors for various lens objects in different gravity models (e.g., Einstein–Gauss–Bonnet (EGB) gravity, Horndeski gravity). The astrophysical consequences regarding the image position, separation, magnification, Einstein ring, and time delays in the formation of relativistic images have also been investigated in the context of various supermassive BHs (Man & Cheng 2014; Guerrero et al. 2020; Ghosh et al. 2021; Hsieh et al. 2021; Islam & Ghosh 2021; Kumar et al. 2022b, 2020b, 2022a).

Bozza et al. (2001) developed a method to obtain the deflection angle by a massive object (BH) in the strong field limit, and they observed that the deflection angle diverges logarithmically for the Schwarzschild BH. Bozza (2002) also proved that this method is valid for any general asymptotically spherically symmetric spacetime. The strong gravitational phenomena have been applied to a different type of BH, wormhole, and naked singularity spacetime with a photon sphere. Gibbons & Werner (2008) introduced a new approach by applying the Gauss–Bonnet theorem and they applied it to investigate the weak gravitational lensing for the case where the receiver and source are located at an infinite distance from the lens such as Schwarzschild BH. With the help of Gibbons & Werner's method, gravitational lensing, has been widely investigated in the literature (Sakalli & Ovgun 2017; Goulart 2018; Jusufi et al. 2018; Javed et al. 2019a, 2020a; de Leon & Vega 2019). Ishihara et al. (2017, 2016) extended Gibbons & Werner's method to investigate finite-distance gravitational deflection angle in static spherically symmetric spacetime

where the receiver and source are located in finite-distance regions. Later Ono et al. (2017, 2018, 2019) introduced a new optical metric method to extend the investigation for stationary axially symmetric spacetime. Furthermore, finite-distance deflection angles have been investigated by other authors (Arakida 2018; Crisnejo et al. 2019b; Haroon et al. 2019; Ono & Asada 2019; Li & Jia 2020; Li & Ovgun 2020). Gravitational lensing effects induced by various BHs have been studied numerically and analytically in the strong field limit as well as weak field limit (Zhao & Xie 2016; Pang & Jia 2019; Mustafa et al. 2022; Qiao & Zhou 2022). Islam et al. (2021) investigated gravitational lensing by rotating a Simpson–Visser BH in the strong field limit. They discussed the astrophysical consequences using a supermassive BH and showed that rotating a Simpson–Visser BH can be distinguished from a Kerr BH via strong gravitational lensing effects. Kumar et al. (2022a) studied the strong gravitational lensing effect by a hairy BH in Horndeski's theory of gravity. They discussed the astrophysical consequences of various supermassive BHs, due to the hairy BH in Horndeski's theory of gravity and compared it with the standard Schwarzschild BH in GR. Recently, Islam et al. (2022) investigated the strong gravitational lensing effect, due to the Bardeen BH in four-dimensional Einstein–Gauss–Bonnet (EGB) gravity. They also studied the astrophysical consequences via strong gravitational lensing effect by taking the example of various supermassive BHs with 4D EGB Bardeen BHs and compared them to the standard Schwarzschild and Bardeen BHs. Kumar et al. (2022b) explored gravitational lensing by regular electrically charged (REC) BH spacetime as well as REC no-horizon spacetime in the strong field limit. They investigated the astrophysical consequences for various supermassive BHs with regular spacetime and compared them with the standard Schwarzschild BH. Using the Gauss–Bonnet theorem, Kumar et al. (2020a) evaluated the weak deflection of light, due to the rotating Kalb–Ramond BH where the observer and source are located at the finite-distance region. They analyzed the effect of the Kalb–Ramond field on the rotating BH spacetime geometry and numerically deduced corrections to the light deflection angle from Schwarzschild as well as Kerr BH values.

Motivated by the above ideas, we study the acoustic BH with charges via gravitational lensing for both weak and strong field regimes in the present paper. The BH is one of the most significant predictions in GR. In 2015, gravitational waves from the merging of a binary system of BHs were detected by the Ligo and Virgo collaborations (Abbott et al. 2016), and in 2019, the first image of the shadow of a BH at the center of galaxies was observed by the Event-Horizon-telescope collaboration (Akiyama et al. 2019a, 2019b). These two strong observations have provided us with proof of the existence of a BH in our universe. However, there have been a lot of remarkable observations that have resulted in progress in BH physics and other branches of physics. In the last decade, a new type of analogous object, the acoustic BH, has been developed and investigated, which provides a potential connection between astrophysical BH and tabletop experiments (Unruh 1981). Acoustic BHs with different systems (models) have been constructed and studied (e.g., Ge & Sin 2010; Anacleto et al. 2011, 2012; Ge et al. 2012, 2015, 2019). Moreover, acoustic BHs have been studied for various astrophysical aspects such as shadows, light deflection angle, Unruh effect, quasinormal moles, quasi-bound states, quasi-particle propagation, and Hawking radiation, etc. (Fischer & Visser 2002, 2003; Cardoso et al. 2004; Benone et al. 2015; Eskin 2019; Lima et al. 2019; Guo et al. 2020; Ling et al. 2021; Vieira & Kokkotas 2021). Ling et al. (2021) constructed the curve of the acoustic BH with charges. They also investigated the shadow and near-horizon structure of this type of BH. Recently, Qiao & Zhou (2021) investigated the gravitational lensing of the acoustic Schwarzschild BH by applying the Gauss–Bonnet theorem and geodesic methods.

In this work, we investigate gravitational lensing by an acoustic charged BH both in strong and weak field approximations and assess the phenomenological differences between a Reissner–Nordström BH ($\xi = 0$) and a standard Schwarzschild BH ($\xi = 0$, $Q = 0$), in particular, the effect of tuning parameter ξ and charged parameter Q on the strong lensing observables, Einstein ring, and the time delay between the relativistic images. In the investigation of gravitational lensing, we mainly apply two methods. One is is a useful method developed by Bozza (2003) in the strong field regime, and the other is Gibbons & Werner (2008)'s method using the Gauss–Bonnet theorem in the weak field regime. We investigate the strong gravitational lensing via. analyzing null geodesics by the acoustic charged BH in curve spacetime. Considering the various supermassive BHs at the center of galaxies, we obtain the strong lensing observable in the image position, separation and magnification, Einstein ring, and time delays in the formation of relativistic images.

This paper is presented as follows. In Section 2, we review the acoustic charged BH in curve spacetime and derive its null geodesics. In Section 3, we discuss the strong gravitational lensing by an acoustic charged BH. Furthermore, strong lensing observables, including image position, separation, magnification, Einstein's ring, and time delays of the relativistic images, are analyzed. Section 4 is devoted to studying the weak gravitational lensing by an acoustic charged BH for the case where the receiver and source are located at the infinite-distance region. Estimations of observables considering the BH having a mass of $\boldsymbol{M} = 2.8 \times 10^6$ and distance $\boldsymbol{D_{ol}} = 8.5$ Kpc, and a comparison of the results of the observables among astrophysical BHs (Schwarzschild and Reissner–Nordström) and acoustic BHs (acoustic Schwarzschild, acoustic charged) are also given in Section 5.

Finally, we summarize our results and conclude in Section 6. We briefly discuss the weak gravitational lensing by acoustic charged BH for the case where the receiver and source are located at the finite-distance region in the Appendix.

2. Acoustic Charged BH and Null Geodesics

The static, spherically symmetric acoustic charged BH in curved spacetime is described by Ling et al. (2021) as

$$ds^2 = -f(r)dt^2 + \frac{1}{f(r)}dr^2 + r^2(d\theta^2 + \sin^2\theta d\phi^2), \quad (1)$$

where

$$f(r) = \left(1 - \frac{2M}{r} + \frac{Q^2}{r^2}\right)\left[1 - \xi\left(1 - \frac{2M}{r} + \frac{Q^2}{r^2}\right)\right] \times \left(1 - \frac{2M}{r} + \frac{Q^2}{r^2}\right). \quad (2)$$

Here, M and Q are the mass and charge of the acoustic charged BH, respectively. The parameter ξ is known as the tuning parameter, which is strongly related to the radial velocity v_r of moving fluid via $v_r = \sqrt{\left(\frac{2M}{r} - \frac{Q^2}{r^2}\right)\xi}$. The radial velocity component v_r is real when tuning parameter $\xi \geqslant 0$. It is also known that the radial velocity v_r for a static observer with radial position r is always greater than the escape velocity $v_e = \sqrt{\left(\frac{2M}{r} - \frac{Q^2}{r^2}\right)}$. Thus, the tuning parameter must satisfy $\xi \geqslant 0$ such that the relativistic fluid can move around the BH. When $\xi \to \infty$, the radial velocity $v_r \to \infty$, and hence, the acoustic charged BH covers the whole spacetime. In the absence of tuning parameter ξ, the spacetime, Equation (1), reduces to a Reissner–Nordström BH. Further, $Q = 0$ and $Q = 0$, $\xi = 0$ yield acoustic Schwarzschild and standard Schwarzschild BHs. The horizons of the acoustic charged BH can be obtained by solving $f(r) = 0$ and have been discussed in detail in Ling et al. (2021).

The Lagrangian equation in the equatorial plane $\theta = \frac{\pi}{2}$ for a photon traveling around the acoustic charged BH is given by

$$-\left(1 - \frac{2M}{r} + \frac{Q^2}{r^2}\right)\left[1 - \xi\left(1 - \frac{2M}{r} + \frac{Q^2}{r^2}\right)\right] \times \left(1 - \frac{2M}{r} + \frac{Q^2}{r^2}\right)\dot{t}^2 + \frac{\dot{r}^2}{\left(1 - \frac{2M}{r} + \frac{Q^2}{r^2}\right)\left[1 - \xi\left(1 - \frac{2M}{r} + \frac{Q^2}{r^2}\right)\right]\left(1 - \frac{2M}{r} + \frac{Q^2}{r^2}\right)} + r^2\dot{\phi}^2 = \epsilon,$$

where $\epsilon = -1, 0, 1$ correspond to the case of space-like, null, and time-like geodesics. Using Equation (3), null geodesics with respect to affine parameter λ can be obtained by the following equations:

$$\dot{t} = \frac{dt}{d\lambda} = \frac{E}{\left(1 - \frac{2M}{r} + \frac{Q^2}{r^2}\right)\left[1 - \xi\left(1 - \frac{2M}{r} + \frac{Q^2}{r^2}\right)\right]\left(1 - \frac{2M}{r} + \frac{Q^2}{r^2}\right)} \tag{4}$$

$$\dot{\phi} = \frac{d\phi}{d\lambda} = \frac{L}{r^2} \tag{5}$$

$$\dot{r} = \frac{dr}{d\lambda} = \sqrt{E^2 - \frac{L^2}{r^2}f(r)}, \tag{6}$$

where the constants E and L are the energy angular momentum of the particle and the function $f(r)$ is given by Equation (2).

3. Strong Gravitational Lensing by Acoustic Charged BH

Here, we study the strong gravitational lensing in an acoustic charged BH by null geodesics to investigate how the charged parameter Q affects the strong lensing observables and compare it to the Reissner–Nordström BH ($\xi = 0$) as well as the Schwarzschild BH ($\xi = 0$, $Q = 0$).

Here, we investigate the deflection of photon rays in the equatorial plane ($\theta = \frac{\pi}{2}$), due to an acoustic charged BH. To study the deflection angle of photon rays in the equatorial plane ($\theta = \frac{\pi}{2}$), we write Equation (1) in terms of Schwarzschild radius by the transformations, $t \to \frac{t}{2M}$, $r \to \frac{r}{2M}$, $Q \to \frac{Q}{2M}$ as

$$d\bar{s}^2 = -A(r)dt^2 + B(r)dr^2 + C(r)d\phi^2, \tag{7}$$

where

$$A(r) = \left(1 - \frac{1}{r} + \frac{Q^2}{r^2}\right)\left[1 - \xi\left(1 - \frac{1}{r} + \frac{Q^2}{r^2}\right)\right] \times \left(1 - \frac{1}{r} + \frac{Q^2}{r^2}\right),$$

$$B(r) = \left\{\left(1 - \frac{1}{r} + \frac{Q^2}{r^2}\right)\left[1 - \xi\left(1 - \frac{1}{r} + \frac{Q^2}{r^2}\right)\right] \times \left(1 - \frac{1}{r} + \frac{Q^2}{r^2}\right)\right\}^{-1}$$

and

$$C(r) = r^2.$$

Equation (6) can be written as

$$\left(\frac{dr}{d\lambda}\right)^2 + V_{\text{eff}} = E^2, \tag{8}$$

where the effective potential of the photon is given by

$$V_{\text{eff}} = \frac{L^2}{r^2}A(r). \tag{9}$$

For the unstable circular photon orbit of radius r_c, the conditions for the effective potentials are $\frac{dV_{\text{eff}}}{dr}|_{r_c} = 0$ and $\frac{d^2V_{\text{eff}}}{dr^2}|_{r_c} < 0$. Thus, the radius of the photon sphere r_c is the largest real root of the equation

$$2A(r_c) - r_cA'(r_c) = 0. \tag{10}$$

Note that at $r = r_c$, the condition $\frac{d^2V_{\text{eff}}}{dr^2}|_{r_c} < 0$ is satisfied for the acoustic charge BH. Since the orbits are unstable against small perturbations. Thus, the photons coming from infinity to the BH with some impact parameter u with the closest distance r_0 get back to infinity. When the particle reaches its minimal distance r_0 closest to the central BH, where $\frac{dr}{d\lambda} = 0$, we have the ratio $\frac{L}{E}$ as an impact parameter u in terms of closest distance r_0 (Bozza 2002).

$$u = \frac{L}{E} = \frac{r_0}{\sqrt{A(r_0)}}. \tag{11}$$

Figure 1 (a) describes the behavior of the photon sphere radius r_c with the charged parameter Q for the different values of tuning parameter ξ. In this Figure, we can see that for the fixed value of charge parameter Q the radius of the photon sphere r_c increases with the increasing tuning parameter ξ. We also observe that when $\xi = 0$ and $Q = 0$, $r_c = 1.5$ (yellow solid line) corresponds to the case of a Schwarzschild BH (Bozza 2002).

When $r_0 \to r_c$, a strong deflection angle becomes unboundedly large and for $r_0 > r_c$, it is finite only. Thus, the critical

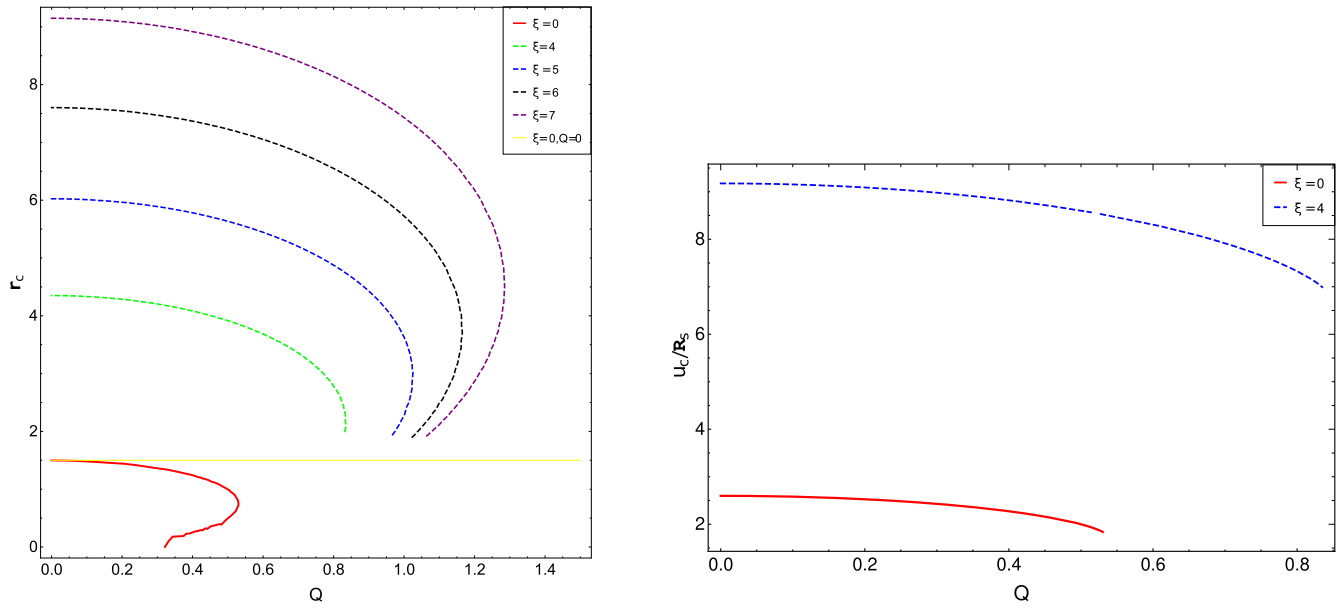

Figure 1. Panel (a): the behavior of the photon sphere radius r_c with the charge parameter Q for different values of tuning parameters $\xi = 0, 4, 5, 6, 7$ for the acoustic charged BH and the yellow solid line represents the photon sphere radius of a Schwarzschild ($\xi = 0$, $Q = 0$) BH. Panel (b): the behavior of the critical impact parameter u_c at $r = r_c$ with the charge parameter Q for different values of tuning parameter $\xi = 0, 4$.

impact parameter u_c is given by

$$u_c = \frac{r_c}{\sqrt{A(r_c)}}. \tag{12}$$

When the impact parameter is $u < u_c$, photons fall into the BH, and if the impact parameter is $u > u_c$, photons reach the closest distance r_0 near the BH, but when the impact parameter is $u = u_c$, photons revolve around the BH in an unstable circular orbit, and hence, create a photon sphere of radius r_c.

Figure 1(b) describes the behavior of the critical impact parameter u_c with the charged parameter Q for the different values of tuning parameters $\xi = 0, 4$. In this figure, we can see that for the fixed value of tuning parameter ξ, the critical impact parameter u_c decreases with the increasing magnitude of charge parameter Q. We also observe that when $\xi = 0$ and $Q = 0$, $u_c/R_s = 2.59808$ corresponds to the case of a Schwarzschild BH (Bozza 2002).

Using the equation, the deflection angle in the strong field limit for the acoustic charged BH spacetime can be defined as (Claudel et al. 2001; Virbhadra & Ellis 2002)

$$\alpha_D(r_0) = I(r_0) - \pi, \tag{13}$$

where r_0 is the closest approach distance of the photons' trajectory and $I(r_0)$ is defined as

$$I(r_0) = 2\int_{r_0}^{\infty} \frac{d\phi}{dr} dr, \tag{14}$$

or

$$I(r_0) = \int_{r_0}^{\infty} \frac{2\sqrt{B(r)}\, dr}{\sqrt{C(r)}\sqrt{\frac{A(r_0)C(r)}{A(r)C(r_0)} - 1}} dr. \tag{15}$$

The deflection angle $\alpha_D(r_0)$ in the strong field limit depends upon the relation between r_0 and r_c and when $r_0 \approx r_c$, it is increased. So, we introduce a new variable z as (Bozza 2003)

$$z = \frac{A(r) - A(r_0))}{1 - A(r_0)}. \tag{16}$$

The total azimuthal angle in terms of new variables can be written as

$$\phi(r_0) = \int_0^1 F(z, r_0) R(z, r_0) dz, \tag{17}$$

where

$$F(z, r_0) = \frac{2(1 - A(r_0))\sqrt{C(r_0)}}{C(r)A'(r)} \sqrt{A(r)B(r)|A(r_0)|}, \tag{18}$$

$$R(z, r_0) = \frac{\sqrt{C(r)}}{\sqrt{sgn(A(r_0))(C(r)A(r_0) - A(r)C(r_0))}}. \tag{19}$$

The metric coefficients other than subscript "0" are formulated at $r = A(r)^{-1}(1 - A(r_0))z + A(r_0))$. For all values of z and r_0, the function $F(z, r_0)$ becomes regular but the function $R(z, r_0)$ diverges at $z = 0$ only.

The integral (17) can be expressed as

$$\phi(r_0) = \phi^D(r_0) + \phi^R(r_0) \tag{20}$$

with the regular part

$$\phi^R(r_0) = \int_0^1 g(z, r_0) dz \tag{21}$$

and the divergent part

$$\phi^D(r_0) = \int_0^1 F(z, r_c) R_0(z, r_0) dz, \tag{22}$$

where $g(z, r_0) = F(z, r_0)R(z, r_0) - F(0, r_c)R_0(z, r_0)$. To obtain the divergence of the integrand in Equation (22), one can

expand the portion of the square root in $R(z, r_0)$ as

$$R_0(z, r_0) = \frac{1}{\sqrt{p(r_0)z + q(r_0)z^2 + \mathcal{O}(z^3)}}, \tag{23}$$

where

$$p(r_0) = sgn(A(r_0))\frac{(1 - A(r_0))}{A'(r_0)C(r_0)} \times (A(r_0)C'(r_0) - A'(r_0)C(r_0)), \tag{24}$$

$$q(r_0) = \frac{(1 - A(r_0))^2}{A'^3(r_0)C^2(r_0)}(2C(r_0)C'(r_0)A'(r_0)^2 + (C(r_0)C''(r_0) - 2C'^2(r_0))A(r_0)A'(r_0) - C(r_0)C'(r_0)A(r_0)A''(r_0). \tag{25}$$

Here, prime denotes the derivative with respect to r. When $r_0 \approx r_c$, the coefficients $p(r_0)$ vanish and the order of divergence is z^{-1}, which leads to the integral divergence logarithmically.

For $r_0 \approx r_c$, the strong deflection angle becomes

$$\alpha(u) = -\bar{a}\log\left(\frac{u}{u_c} - 1\right) + \bar{b} + \mathcal{O}(u - u_c), \tag{26}$$

where

$$\bar{a} = \frac{F(0, r_c)}{2\sqrt{q(r_c)}} = \sqrt{\frac{2A(r_c)B(r_c)}{A(r_c)C''(r_c) - A''(r_c)C(r_c)}} \tag{27}$$

and

$$\bar{b} = -\pi + a_R + \bar{a}\log\left(\frac{4\zeta(r_c)A(r_c)}{u_c|A(r_c)|(2u_cA(r_c))}\right), \tag{28}$$

$a_R = \phi^R(r_c) = \int_0^1 g(z, r_c)dz$, which is numerically obtained.

We numerically evaluate the critical impact parameter u_c and the lensing coefficients $\bar{a}$ and $\bar{b}$ in the strong field limit with the tuning parameters $\xi = 0, 4, 5$ with the different values of charge parameter Q, which are shown in Table 1. In this table, we can see that for the fixed value of tuning parameter ξ (= 0, 4, 5) strong lensing coefficients $\bar{a}$ grow with increasing magnitude of charged parameter Q while the strong lensing coefficient $\bar{b}$ grows at first and reaches the maximum value and then decreases. When $\xi = 0$ and $Q = 0$, the value of the strong lensing coefficients $\bar{a} = 1$ and $\bar{b} = -0.40023$ corresponds to the case of the Schwarzschild BH (Bozza 2002). The strong deflection angle α_D for the acoustic charged BH is displayed in Figure 2(a) and (b) decreases with the impact parameter u for the different magnitudes of charged parameter Q and also $\alpha_D \to \infty$ as $u \to u_c$. In Figure 2(c), we can see that for the fixed value of tuning parameters $\xi = 0, 4$, the strong deflection angle for acoustic charged BH increases with the increasing magnitude of charged parameter Q. In Figure 2(c), we can also observe that strong deflection angle α_D for the acoustic charged BH ($\xi = 4$) is greater than the Reissner–Nordström BH ($\xi = 0$) as well as for the Schwarzschild BH ($\xi = 0$, $Q = 0$). The acoustic charged BH, with the presence of tuning parameter ξ, can greatly intensify the gravitational lensing effect compared to the other BHs. This result indicates that the gravitational lensing effect, due to acoustic charged BH, is greatly enhanced compared to ordinary astrophysical BHs. Thus, acoustic charged BHs with the presence of moving fluid and sound waves can be detected more easily and distinguished from ordinary astrophysical BHs.

Table 1
Estimation of Strong Lensing Coefficients with Different Values of ξ and Q

	Strong Lensing Coefficients			
ξ	$\|Q\|$	$\bar{a}$	$\bar{b}$	u_c/R_s
0	0	1.00	−0.40023	2.59808
	0.05	1.0012	−0.400004	2.59374
	0.1	1.00456	−.399348	2.58062
	0.2	1.01974	−0.397184	2.52649
	0.3	1.05183	−0.396509	2.42935
	0.4	1.12317	−0.413638	2.27299
	0.5	1.41421	−0.733203	2.00
4	0	1.58592	−0.881075	9.17557
	0.05	1.58694	−0.881771	9.17029
	0.1	1.59003	−0.883895	9.15441
	0.2	1.6029	−0.892955	9.09019
	0.3	1.62623	−0.910361	8.98042
	0.4	1.66372	−0.940932	8.82042
	0.5	1.72303	−0.995824	8.60195
5	0.05	1.33284	−0.533293	11.8853
	0.1	1.33426	−0.533429	11.8704
	0.2	1.3401	−0.534054	11.8106
	0.3	1.35037	−0.535422	11.7092
	0.4	1.36604	−0.538163	11.5634
	0.5	1.38882	−0.543562	11.3686

3.1. Strong Lensing Observables

Next, we investigate the various observables of strong lensing by acoustic charge BH. Here, we consider the case where the source, black hole (lens), and receiver are perfectly aligned, and the receiver and source are located very far from the BH (lens). Thus, the lens equation can be expressed as (Bozza et al. 2001)

$$\gamma = \alpha - \frac{d_{ls}}{d_{os}}\Delta\alpha_n, \tag{29}$$

where γ and α are the angular positions of the image and source, respectively, from the optic axis, and d_{ls}, d_{ol},d_{os} are the lens-source, receiver-lens, and receiver-source distance, respectively, such that $d_{os} = d_{ol} + d_{ls}$.

Here, we consider $\Delta\alpha_n = \alpha - 2n\pi$ as the offset angle and n represents the number of loops of the light ray.

Using Equations (26) and (29), the angular separation between the nth relativistic and the BH (lens) can be written as

$$\theta_n = \theta_n^0 - \frac{u_c e_n d_{os}(\theta_n^0 - \gamma)}{\bar{a}d_{ls}d_{ol}}, \tag{30}$$

where

$$e_n = e^{\frac{\bar{b} - 2n\pi}{\bar{a}}},$$
$$\theta_n^0 = \frac{u_c(1 + e_n)}{d_{ol}},$$

θ_n^0 is the image position for $\alpha = 2n\pi$. For the nth relativistic image, the magnification is defined as (Bozza 2002)

$$\mu_n = \left(\frac{\gamma}{\alpha}\frac{d\gamma}{d\alpha}\right)^{-1}\Bigg|_{\theta_0} = \frac{e_n u_c^2(1 + e_n)d_{os}}{\bar{a}\gamma d_{ls}d_{ol}^2}. \tag{31}$$

It is clear that the first relativistic image is the brightest, and the magnification decreases exponentially with n. Note that as

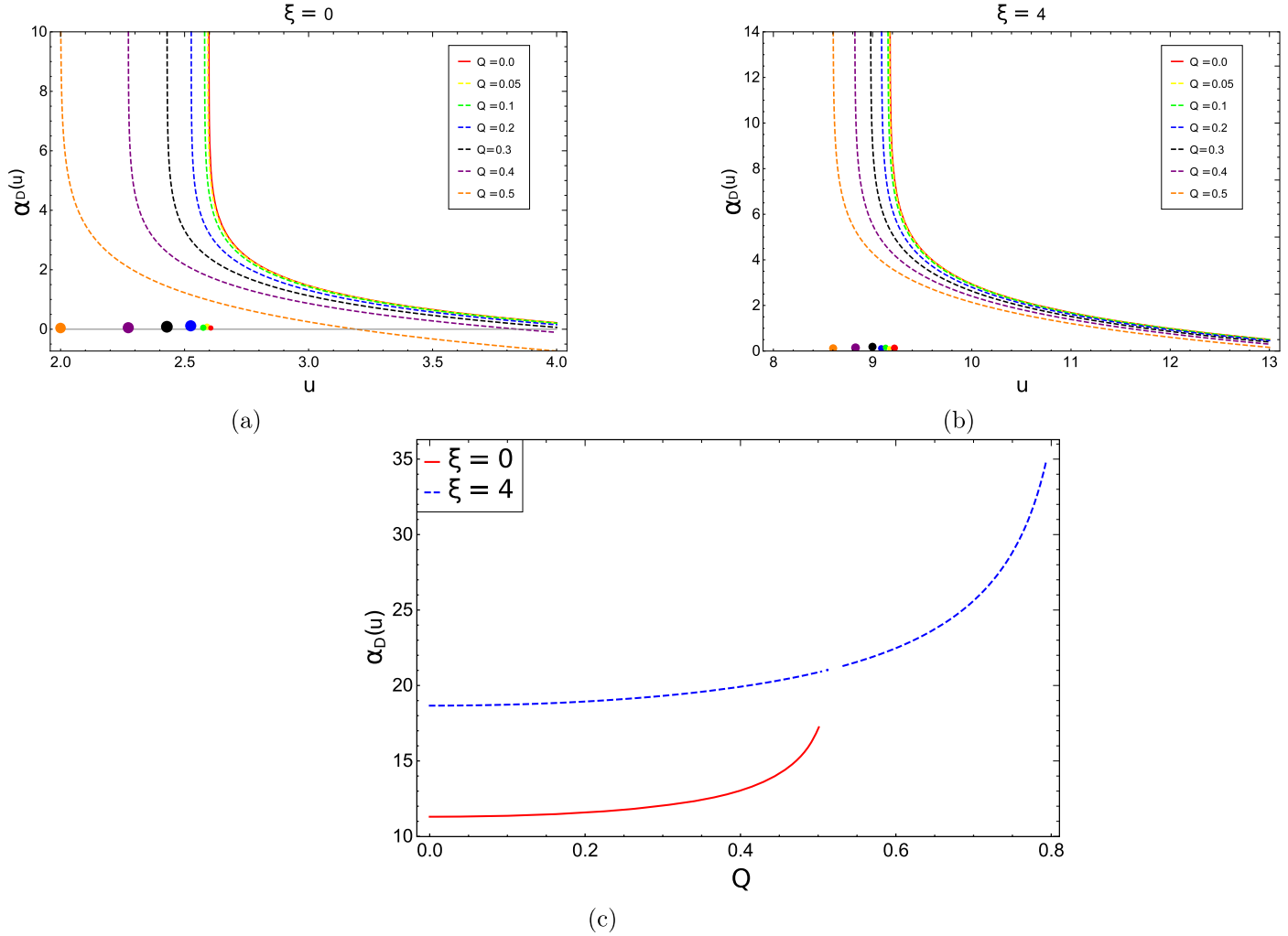

Figure 2. Deflection angle $\alpha_D(u)$ as a function of impact parameter u for $\xi = 0$, 4 (upper panels (a), (b)) and function of charge parameter Q (lower panel (c)) at $u = u_c + 0.00002$. The points on the horizontal lines indicate the value of the impact parameter $u = u_c$, where the deflection angle $\alpha_D(u)$ diverges.

$\gamma \to 0$, Equation (31) diverges; thus, perfect alignment maximizes the possibility of detecting the images.

If $\theta_n|_{n\to\infty} =: \theta_\infty$, it is considered as an asymptotic position of packed of images, then only the brightest image, i.e., the outermost image θ_1 is resolved as a single image, and all the other images are packed together at θ_∞ where θ_∞ is the asymptotic position of the set of relativistic images obtained in the limit $n \to \infty$.

Using the deflection angle, Equation (26), and the lens, Equation (29), we obtained three quantities of observables (see Table 2) such as the asymptotic position of the set of images θ_∞, angular separation X between the outermost image and remaining inner set of images, and the ratio of the flux between the outermost relativistic image and the remaining inner set of relativistic images can be expressed as (Bozza 2002; Kumar et al. 2022b).

$$\theta_\infty = \frac{u_c}{d_{\rm ol}}, \tag{32}$$

$$X = \theta_1 - \theta_\infty \approx \theta_\infty e^{\frac{(\bar{b}-2\pi)}{\bar{a}}}, \tag{33}$$

$$r_{\rm mag} = \frac{\mu_1}{\sum_{n=2}^{\infty}\mu_n} \approx \frac{5\pi}{\bar{a}\log(10)}. \tag{34}$$

If the quantities of the observables X, θ_∞, and $r_{\rm mag}$ are available from the observation, the lensing coefficients $\bar{a}$, $\bar{b}$ and the critical impact parameter u_c in the strong field limit can be obtained easily by Equations (32)–(34) and also compared to the theoretical models' values. Thus, we can identify the nature of the acoustic charged BH (lens).

Considering the supermassive BHs M87*, SgrA*, and NGC 4649 in the nearby galaxies, we compute the quantities of the observables X, θ_∞, and $r_{\rm mag}$ in the context of an acoustic charged BH. The mass and distance from Earth for M87* (Akiyama et al. 2019a) are $M \approx 6.5 \times 10^9 M_\odot$ and $d_{\rm ol} \approx 16.8$ Mpc, for SgrA* they are $M \approx 4.28 \times 10^6\ M_\odot$ and $d_{\rm ol} \approx 8.32$ kpc (Gillessen et al. 2017), and for NGC 4649 they are $M \approx 4.72 \times 10^9 M_\odot$ and $d_{\rm ol} \approx 16.46$ Mpc (Kormendy & Ho 2013).

3.2. Einstein Ring

When the BH (lens), source, and receiver are perfectly aligned, i.e., when $\gamma = 0$, the light rays are deflected equally in all directions by the BH (lens) such that a ring-shaped image is formed, and is known as an Einstein ring (Einstein 1936; Liebes 1964; Mellier 1999; Bartelmann & Schneider 2001; Schmidt 2008; Guzik et al. 2010).

Table 2
Estimation of Strong Lensing Observables for Supermassive BHs M87*, SgrA*, and NGC 4649 with Different Values of ξ and Q

Parameters		M87*		SgrA*		NGC 4649		M87*, SgrA*, NGC 4649
ξ	$\lvert Q\rvert$	$\theta_\infty(\mu as)$	$X(\mu as)$	$\theta_\infty(\mu as)$	$X(\mu as)$	$\theta_\infty(\mu as)$	$X(\mu as)$	r_{mag}
0	0	19.7823	0.0247574	26.3022	0.0329171	14.6617	0.0183491	6.82188
	0.05	19.7492	0.0249205	26.2583	0.0331339	14.6372	0.0184699	6.81371
	0.1	19.6493	0.0253708	26.1255	0.0337327	14.5632	0.0188037	6.79092
	0.2	19.2372	0.0274825	25.5775	0.0365403	14.2577	0.0203687	6.68982
	0.3	18.4975	0.0322929	24.594	0.0429361	13.7095	0.023934	6.48573
	0.4	17.307	0.0445421	23.0111	0.0592225	12.8271	0.0330125	6.07377
	0.5	15.2284	0.106652	20.2474	0.141802	11.2866	0.0790452	4.82381
4	0	69.8645	0.762725	92.8908	1.01411	51.7803	0.565296	4.30153
	0.05	69.8243	0.764167	92.8374	1.01603	51.7505	0.566365	4.29876
	0.1	69.7034	0.768539	92.6766	1.02184	51.6609	0.569605	4.29041
	0.2	69.2144	0.786813	92.0265	1.04614	51.2985	0.583149	4.25596
	0.3	68.3786	0.82005	90.9152	1.09033	50.679	0.607783	4.19491
	0.4	67.1603	0.873659	89.2954	1.16161	49.7761	0.647516	4.10038
	0.5	65.4968	0.958354	87.0837	1.27421	48.5432	0.710287	3.95924
5	0.05	90.4969	0.54393	120.323	0.723201	67.0721	0.403135	5.11831
	0.1	90.3834	0.546157	120.173	0.726162	66.988	0.404786	5.11286
	0.2	89.9281	0.55538	119.567	0.738426	66.6505	0.411622	5.09058
	0.3	89.156	0.571753	118.541	0.760195	66.0783	0.423757	5.05186
	0.4	88.0459	0.5971053	117.065	0.793902	65.2555	0.442546	4.99391
	0.5	86.5626	0.63468	115.092	0.843862	64.1562	0.470396	4.912

Note. The observable quantity r_{mag} does not depend on the mass BH or distance of the BH from the receiver.

Simplifying Equation (30) for $\gamma = 0$, the angular radius of the nth relativistic images is obtained in the form

$$\theta_n = \theta_n^0\left(1 - \frac{u_c e_n d_{os}}{\bar{a} d_{ls} d_{ol}}\right). \tag{35}$$

Considering the case where the BH (lens) is midway between the source and receiver i.e., $d_{os} = 2d_{ol}$ and taking $d_{ol} >> u_c$, the angular radius of the nth relativistic Einstein ring can be obtained as

$$\theta_n^E = \frac{u_c(1 + e_n)}{d_{ol}}. \tag{36}$$

The angular radius θ_1^E represents the outermost Einstein ring and is displayed in Figure 3 for the supermassive BHs SgrA* and M87*.

Figure 3 shows that for the fixed tuning parameter ($\xi = 0\, or\, 4$), the angular radius of the outermost Einstein rings decreases with the increasing magnitude of the charged parameter Q for both the BHs SgrA* and M87*.

3.3. Time Delay in the Strong Field Limit

The time travel by the photon path for the different relativistic images is different, so there is a time difference between the different images. Time delay is another important observable, which can be obtained by the time difference between the formation of images. If the time signal of the first and second images is distinguished in the observation, one can obtain the time delay of the two signals (Bozza & Mancini 2004). When a photon travels in a path to reach an observer from the source, the time taken by a photon around the BH is given by Bozza & Mancini (2004) as

$$\tilde{T} = \tilde{a}\log\left(\frac{u}{u_c} - 1\right) + \tilde{b} + \mathcal{O}(u - u_c). \tag{37}$$

Using Equation (37), one can evaluate the time difference between the two relativistic images.

For spherically symmetric spacetime, the time delay between two images when the images are on the same side of the BH is given by

$$\Delta T_{2,1} = 2\pi u_c = 2\pi D_{ol}\theta_\infty. \tag{38}$$

Using the above equation, if we can evaluate the time delay $\Delta T_{2,1}$ between two images with an accuracy of 2% and critical impact parameter u_c with negligible error, we can obtain the BH distance with an accuracy of 2%. In Table 3, we estimate the time delay $\Delta T_{2,1}$ for various supermassive BHs in the context of the acoustic charged BH ($\xi = 5$, $Q = 0.05$), acoustic Schwarzschild ($Q = 0$, $\xi = 4$), and standard Schwarzschild ($\xi = 0$, $Q = 0$) BH spacetimes.

4. Weak Gravitational Lensing by Acoustic Charged BH

In this section, we investigate the weak gravitational lensing by the acoustic charged BH. The weak deflection angle is derived from the Gauss–Bonnet theorem in the cases where the observer and source are located at an infinite distance from the lens (BH) and the case for the finite-distance region where the receiver and source are located at a finite distance from the BH (lens) is discussed in the Appendix. To calculate the weak deflection angle, Gibbons & Werner (2008) proposed a new method by using the Gauss–Bonnet theorem. Gibbons & Werner's method has been applied to the BH as well as to the wormhole (Werner 2012; Jusufi 2017; Crisnejo & Gallo 2018; Jusufi & Ovgun 2018; Jusufi et al. 2019; Ovgun et al. 2019; Li & Ovgun 2020; Li & Zhou 2020) in the literature. Here, we apply this method to calculate the weak deflection angle by acoustic charged BH for the cases where the receiver and source are located at an infinite distance from the BH (lens).

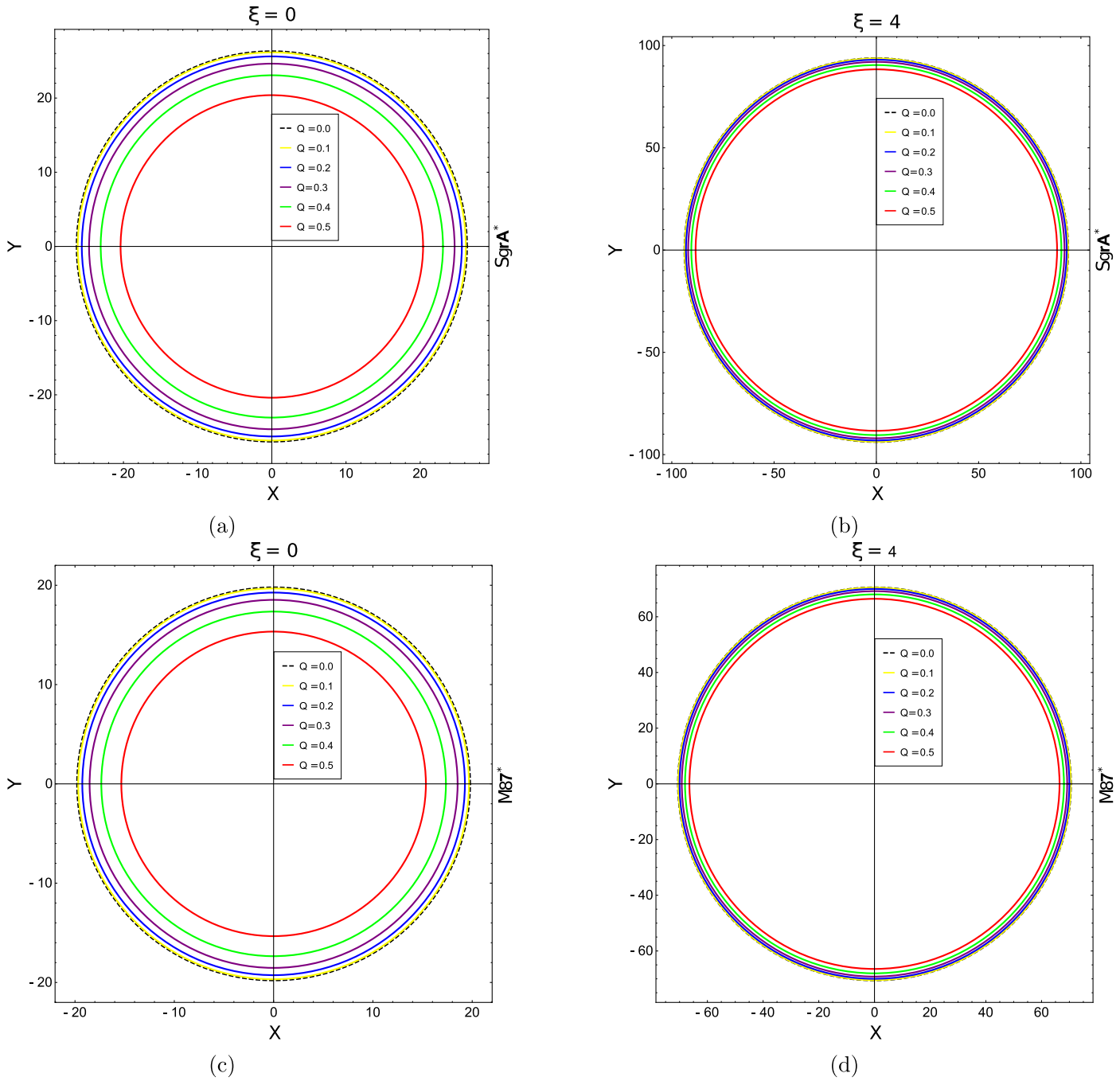

Figure 3. The angular radius θ_n^E of the outermost Einstein ring of an acoustic charged BH as supermassive BHs SgrA* (upper panels (a), (b)) and M87* (lower panels (c), (d)) for $\xi = 0$, 4, respectively.

Gauss–Bonnet theorem states (Gibbons & Werner 2008; Werner 2012) that

$$\int\int_D Kds + \oint_{\partial\mathcal{D}} \kappa_g dl + \sum_i \alpha_i = 2\pi\chi(\mathcal{D}), \tag{39}$$

where ds and dl are the surface element and the line element of the simply connected domain D, and α_i represents the jump angle in the ith vertex of ∂D with a positive sense.

We consider a simple connected domain $D_{r_0} \subset (M, g_{ij})$ by the coordinates (r, ϕ) (see Figure 4), where $\partial D_{r_0} = C_{r_0} \cup \eta_g$ is the boundary of the region D_{r_0}, where η_g is the particle ray from the source to the observer and the curve C_{r_0} is defined by $r = r_0 =$ constant. From Figure 4 we can see the sums of the jump angles $\sum_i^N \alpha_i = \alpha_1 + \alpha_2 \approx \pi$ and the Euler characteristic $\chi(D_{r_0}) = 1$ for the simple connected region D_{r_0}. For the curve C_{r_0}, $\kappa_g(C_{r_0})dl \to d\phi$ is $r_0 \to \infty$, and hence, $\int_{C_\infty} \kappa_g(C_\infty)dl = \int^{\pi+\sigma_\infty} d\phi$, where σ_∞ is the deflection angle for the infinite distance. Thus, the Gauss–Bonnet theorem is stated as

$$\int\int_{D_{r_0}} Kds + \int_S^R d\phi + \alpha_1 + \alpha_2 =^{r\to\infty}$$
$$\int\int_{D_\infty} Kds + \int^{\pi+\sigma_\infty} d\phi + \pi = 2\pi. \tag{40}$$

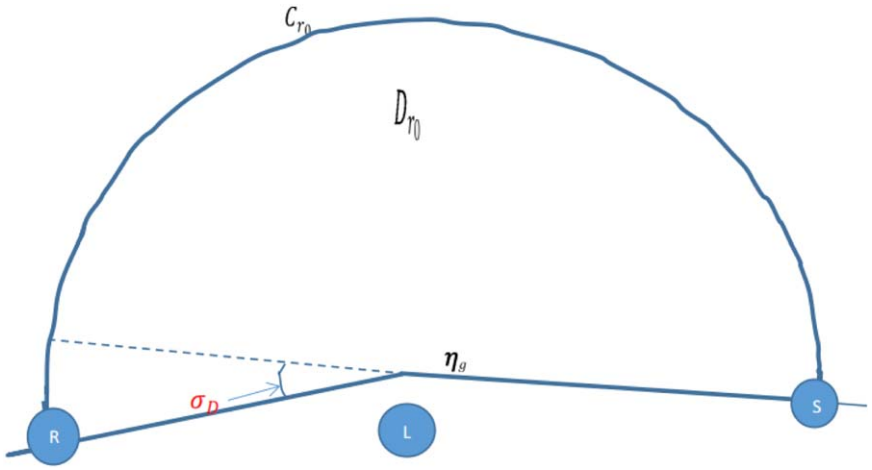

Figure 4. A simply connected domain $D_{r_0} \subset (M, g_{ij})$ with $\partial D_{r_0} = \eta_g \cup C_{r_0}$. The light ray η_g is a geodesic in D_{r_0} and the circular curve C_{r_0} of radius r_0 is considered as $r(\phi) = r_0 =$ constant. R, L, and S denote the observer, the lens (BH), and the source, respectively. The angle σ_D represents the deflection angle for weak gravitational lensing.

Table 3
Estimation of Time Delay for Various Supermassive BHs in the Context of Standard Schwarzschild ($\xi = 0$, $Q = 0$), Acoustic Schwarzschild ($Q = 0$, $\xi = 4$), Reissner–Nordström ($Q = 0.2$, $\xi = 0$), and Acoustic Charged ($\xi = 5$, $Q = 0.05$) BH Spacetimes

Galaxy	$M(M_\odot)$	$D_{\rm ol}$(Mpc)	$\Delta T_{2,1}$ ($\xi = 0$, $Q = 0$)	$\Delta T_{2,1}$ ($\xi = 4$, $Q = 0$)	$\Delta T_{2,1}$ ($\xi = 0$, $Q = 0.2$)	$\Delta T_{2,1}$ ($\xi = 5$, $Q = 0.05$)
Milky Way	4.3×10^6	0.0083	11.4968	40.6029	11.18	52.5937
M87	6.5×10^9	16.68	17,378.9	61,376.5	16,900	79,502.2
NGC 4026	1.80×10^8	13.35	481.261	16,99.66	468	2201.6
NGC 7457	8.95×10^6	12.53	23.9294	84.5107	23.27	109.468
NGC 4395	3.6×10^5	4.3	0.962522	3.39931	0.936	4.4032
NGC 2778	1.45×10^7	23.44	38.7682	136.917	37.7	177.351
NGC 3379	4.16×10^8	10.70	1112.25	3928.09	1081.6	5088.14
NGC 3607	1.37×10^8	22.65	366.293	1293.63	356.2	1675.66
NGC 3842	9.09×10^9	92.2	24,303.7	85,832.6	23634	111181
NGC 4261	5.29×10^8	32.36	1414.37	4995.1	1375.4	6470.25
NGC 4486A	1.44×10^7	18.36	38.5009	135.972	37.44	176.128
NGC 4649	4.72×10^9	16.46	12,619.7	44,568.8	12,272	57,730.8
NGC 4751	2.44×10^9	32.81	6523.76	23,039.8	6344	29,843.9
NGC 5077	8.55×10^8	38.7	2285.99	8073.37	2223	10,457.6
NGC 5516	3.69×10^9	55.3	9865.85	34,842.9	9593.99	45,132.8
NGC 5576	2.73×10^8	25.68	729.912	2577.81	709.8	3339.09
NGC 6251	6.14×10^8	108.4	1641.63	5797.72	1596.4	7509.9
NGC 6861	2.10×10^9	28.71	5614.71	19,829.3	5460	25,685.3
NGC 7052	3.96×10^8	70.4	1058.77	3739.24	1029	4843.52
NGC 7768	1.34×10^9	116.0	3582.72	12,653	3484	16,389.7
Cygnus A	2.66×10^9	242.7	7111.95	2,5117.1	6916	32,534.7

Note. Mass (M) and distance $D_{\rm ol}$ are taken in solar mass and megaparsec units, respectively, and are taken from Kormendy & Ho (2013). Time delays $\Delta T_{2,1}$ are computed in minutes.

Thus, the deflection angle for the cases where both the receiver and source are located very far from the BH can be obtained by

$$\sigma_\infty = -\int\int_{D_\infty} K ds. \tag{41}$$

The acoustic charged BH in curved spacetime (1) can be written as

$$ds^2 = -F(r)dt^2 + (F(r))^{-1}dr^2 + r^2 d\theta^2 + r^2 \sin^2\theta d\phi^2, \tag{42}$$

where

$$F(r) = \left(1 - \frac{2M}{r} + \frac{Q^2}{r^2}\right)\left[1 - \xi\left(1 - \frac{2M}{r} + \frac{Q^2}{r^2}\right)\right] \times \left(1 - \frac{2M}{r} + \frac{Q^2}{r^2}\right). \tag{43}$$

Since the spacetime, Equation (42), is spherically symmetric, the optical spacetime can be written on the equatorial

plane $\frac{\pi}{2}$ as

$$dt^2 = \gamma_{ij}^{\rm op} dx^i dx^j = \frac{dr^2}{F(r)^2} + \frac{r^2 d\phi^2}{F(r)}. \tag{44}$$

Using the metric (42), the Gaussian curvature on the equatorial plane surface can be evaluated as (Werner 2012)

$$\begin{aligned} K &= -\frac{1}{\sqrt{\gamma^{\rm op}}}\left\{\frac{\partial\phi(\partial\phi(\sqrt{\gamma_{rr}^{\rm op}})}{\sqrt{\gamma_{\phi\phi}^{\rm op}}} + \frac{\partial r(\partial r(\sqrt{\gamma_{rr}^{\rm op}})}{\sqrt{\gamma_{rr}^{\rm op}}}\right\} \\ &= -\frac{(F'(r))^2)}{4} + \frac{F(r)F''(r)}{2}, \end{aligned} \tag{45}$$

where $F(r)$ is given by Equation (43). Simplifying Equation (45), one can obtain the Gaussian curvature as follows:

$$\begin{aligned} K = &-\frac{2M(\xi+1)}{r^3} + \frac{3M^2(\xi^2+10\xi+1) + 3Q^2(1+\xi)}{r^4} \\ &- \frac{48M^3\xi(\xi+2) + 6MQ^2(\xi^2+10\xi+1)}{r^5} \\ &+ \frac{8M^4\xi(27\xi+11) + 2Q^2\{Q^2((\xi^2+12\xi+1) + 60M^2(2\xi+1))\}}{r^6} \\ &- \frac{2M\xi(192M^4\xi + 132M^2Q^2 + 87Q^4 + 324M^2Q^2\xi + 42Q^4\xi)}{r^7} \\ &+ \frac{3\xi(80M^6\xi + 90M^2Q^4 + 13Q^6 + 448M^4Q^2\xi + 218M^2Q^4\xi + 6Q^6\xi)}{r^8} \\ &- \frac{Q^2\xi(116MQ^4 + 960M^5\xi + 276MQ^4\xi + 1744M^3Q^2\xi)}{r^9} \\ &+ \frac{6Q^4\xi(3Q^4 + 504M^4\xi + 360M^2Q^2\xi + 7Q^4\xi)}{r^{10}} \\ &- \frac{36MQ^6\xi^2(34M^2+9Q^2)}{r^{11}} + \frac{Q^8\xi^2(543M^2+Q^2)}{r^{12}} \\ &- \frac{126MQ^{10}\xi^2}{r^{13}} + \frac{12Q^{12}\xi^2}{r^{14}}. \end{aligned} \tag{46}$$

And the surface area on the equatorial plane is given by

$$\begin{aligned} dS &= \sqrt{\gamma^{\rm op}}\, dr d\phi = \frac{r}{[F(r)]^{\frac{3}{2}}} dr d\phi \\ &= \left[1 - \frac{3Q^2(\xi+1)}{2r^2} - \frac{3M\{Q^2(5\xi^2+2\xi+5) - 2r^2(1+\xi)\}}{2r^3}\right. \\ &- \frac{3M^2\{Q^2(35\xi^3 - 15\xi^2 + 9\xi + 35) - 2r^2(5\xi^2+2\xi+5)\}}{4r^4} \\ &- \frac{M^3\{15Q^2(21\xi^4 - 28\xi^3 - 2\xi^2 + 4\xi + 21) - 2r^2(35\xi^3 - 15\xi^2 + 9\xi + 35)\}}{4r^5} \\ &\left. + \mathcal{O}\left(\left(\frac{M}{r}\right)^4, \left(\frac{Q}{r}\right)^4\right)\right] r dr d\phi. \end{aligned} \tag{47}$$

According to Gibbons & Werner (2008)'s method, we can calculate the integration, Equation (41), by using the leading order approximation $r(\gamma) = r(\phi) \approx \frac{b}{\sin(\phi)}$, where b is an impact parameter. Thus, for the infinite-distance region, the deflection angle of a

massive particle in the weak field limit can be obtained as

$$\begin{aligned}
\sigma_D &= -\int\int_{D_R} Kds = -\int_{\alpha_S}^{\alpha_o} d\phi \int_{r(\gamma)}^{\infty} K\frac{r}{[F(r)]^{\frac{3}{2}}}dr \\
&= -\int_0^{\pi} d\phi \int_{\frac{b}{\sin\phi}}^{\infty} K\frac{r}{[F(r)]^{\frac{3}{2}}}dr \\
&= -\int_0^{\pi} d\phi \int_{\frac{b}{\sin\phi}}^{\infty} \\
&\left[\frac{3Q^2(1+\xi)}{r^3} + \frac{M\{6Q^2(\xi^2-6\xi+1)-2r^2(1+\xi)\}}{r^4}\right. \\
&+ \frac{M^2\{15Q^2(\xi^3-5\xi^2+3\xi+1)-3r^2(\xi^2-6\xi+1)\}}{r^5} \\
&+ \frac{3M^2\{5Q^2(5\xi^4-28\xi 63+30\xi^2+4\xi+5)-4r^2(\xi^3-5\xi^2+3\xi+1)\}}{2r^6} \\
&\left.+ \mathcal{O}\left(\left(\frac{M}{r}\right)^4,\left(\frac{Q}{r}\right)^4\right)\right]dr \\
&= -\int_0^{\pi} \\
&\left[\frac{3Q^2(1+\xi)\sin^2\phi}{2b^2} + \frac{M\{2Q^2(\xi^2-6\xi+1)\sin^3\phi-2b^2(1+\xi)\sin\phi\}}{b^3}\right. \\
&+ \frac{M^2\{15Q^2(\xi^3-5\xi^2+3\xi+1)\sin^4\phi-6b^2(\xi^2-6\xi+1)\sin^2\phi\}}{4b^4} \\
&+ \frac{3M^3Q^2(5\xi^4-28\xi^3+30\xi^2+4\xi+5)\sin^5\phi}{2b^5} \\
&- \frac{2M^3(\xi^3-5\xi^2+3\xi+1)\sin^3\phi}{b^3} \\
&\left.+ \mathcal{O}\left(\left(\frac{M}{b}\right)^4,\left(\frac{Q}{b}\right)^4\right)\right]d\phi \\
&= -\frac{3\pi Q^2(1+\xi)}{4b^2} - \frac{M\{8Q^2(\xi^2-6\xi+1)-12b^2(1+\xi)\}}{3b^3} \\
&- \frac{M^2\pi\{45Q^2(\xi^3-5\xi^2+3\xi+1)-24b^2(\xi^2-6\xi+1)\}}{32b^4} \\
&- \frac{8M^3Q^2(5\xi^4-28\xi 63+30\xi^2+4\xi+5)}{5b^5} \\
&+ \frac{8M^3(\xi^3-5\xi^2+3\xi+1)}{3b^3} + \mathcal{O}\left(\left(\frac{M}{b}\right)^4,\left(\frac{Q}{b}\right)^4\right).
\end{aligned} \tag{48}$$

Equation (48) can be reduced to the case of an acoustic Schwarzschild BH (Qiao & Zhou 2021) when tuning parameter $Q=0$, a standard Reissner–Nordström BH when $\xi=0$ (Sereno 2004), and a standard Schwarzschild BH when both tuning parameter $\xi=0$ and charged parameter $Q=0$. Thus, the weak deflection angle for the acoustic Schwarzschild $\sigma_D|_{\rm AS}$, standard Reissner–Nordström BH $\sigma_D|_{\rm RN}$, and standard Schwarzschild BH $\sigma_D|_S$ are obtained, respectively, as

$$\begin{aligned}
\sigma_D|_{\rm AS} &= \frac{4M(\xi+1)}{b} + \frac{3M^2\pi(\xi^2-6\xi+1)}{4b^2} \\
&+ \frac{8M^3(\xi^3-5\xi^2+3\xi+1)}{3b^3} + \mathcal{O}\left(\left(\frac{M}{b}\right)^4\right),
\end{aligned} \tag{49}$$

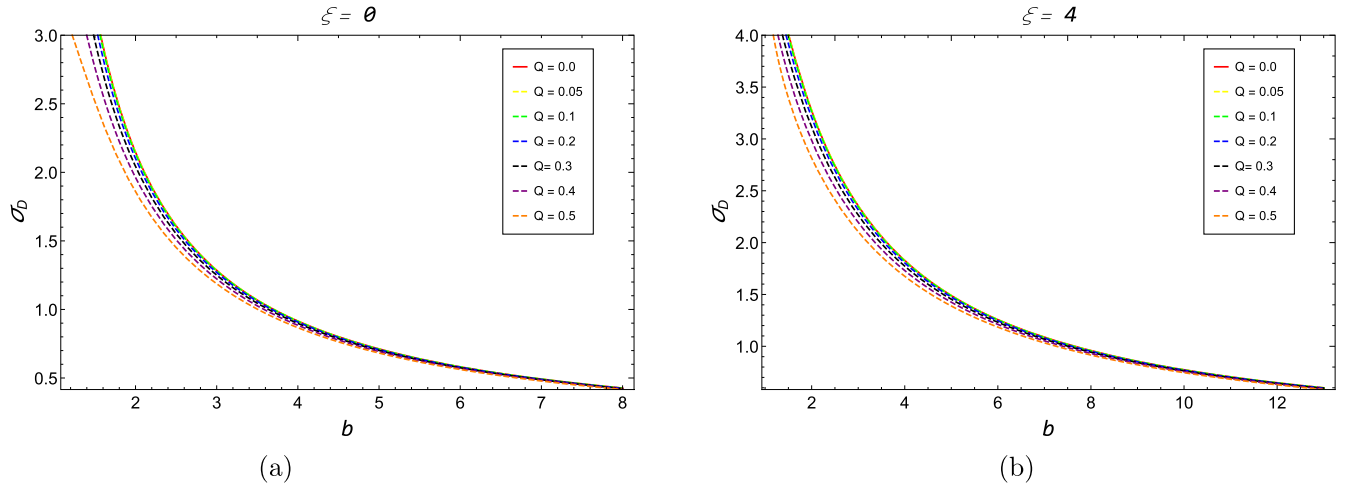

Figure 5. Deflection angle σ_D in the weak field limit as a function of charged parameter Q for the cases of $\xi = 0$ (left panel (a)) and $\xi = 4$ (right panel (d)), respectively.

$$\sigma_D|_{\rm RN} = \frac{4M}{b} - \frac{3\pi(Q^2 - M^2)}{4b^2} + \frac{8M(M^2 - Q^2)}{3b^3} - \frac{45\pi M^2 Q^2}{32b^4} - \frac{8M^3Q^2}{b^5} + \mathcal{O}\left(\left(\frac{M}{b}\right)^4\left(\frac{Q}{b}\right)^4\right) \tag{50}$$

and

$$\sigma_D|_S = \frac{4M}{b} + \frac{3M^2\pi}{4b^2} + \frac{8M^3}{3b^3} + \mathcal{O}\left(\left(\frac{M}{b}\right)^4\right). \tag{51}$$

These observations agree with the analysis in Islam et al. (2020) but the weak deflection angle of the standard Schwarzschild BH $\sigma_D|_S$ corresponds to ($Q = 0$, $\xi = 0$), Equation (48), is not consistent with the results obtained in (Islam et al. 2020), due to the leading order approximation of the particle orbit $r(\gamma) = r(\phi) \approx \frac{b}{\sin(\phi)}$, $u \approx \frac{\sin(\phi)}{b}$ used in the integration (48) instead of higher order approximation (Crisnejo et al. 2019a). In Figure 5, we can see that for the fixed value of charged parameter Q and tuning parameter ξ, the weak deflection angle σ_D decreases with the impact parameter b, and the weak deflection angle σ_D decreases with the increasing magnitude of the charged parameter Q for the fixed value of the tuning parameter ξ. Note that these resultant features also can be acquired in the case of gravitational phenomena for the ordinary astrophysical BH by following the literature (e.g., Sereno 2004; Briet & Hobill 2008; Jusufi 2016; Javed et al. 2020b). With the help of the Gauss–Bonnet theorem, Jha & Rahaman (2022) investigated that the weak deflection angle due to the hairy Schwarzschild BH decreases with the impact parameter b for the fixed value of other parameters. Molla & Debnath (2022) found that the weak deflection angle for the power Maxwell charged BH in Rastall gravity decreases with the impact parameter b for the fixed value of the Maxwell parameter and the Rastall parameter. Javed et al. (2020c) analyzed the graphical behavior of a weak deflection angle for the stringy BH. They have shown that the weak deflection angle due to the stringy BH decreases with the impact parameter b for the fixed value of charge parameter Q.

5. Comparison with Observations

Astrophysical BHs like the Schwarzschild and Reissner–Nordström BHs are a special solution of an acoustic charged BH. Several works have been done to investigate the gravitational lensing effects of the ordinary astrophysical BHs, such as Schwarzschild, Reissner–Nordström, etc., which have been discussed previously. In this work, we extend the Bozza (2002) or other literature analyses (e.g., Virbhadra & Ellis 2000; Bozza & Mancini 2004) for Schwarzschild and Reissner–Nordström BHs and Qiao & Zhou (2021)'s analysis for an acoustic Schwarzschild BH to the case of an acoustic charged BH. The ordinary astrophysical BHs (Schwarzchild and Reissner–Nordström) and the acoustic BHs (acoustic Schwarzschild and acoustic charged) have the same formality, but there is an additional parameter ξ present in acoustic types of spacetime, which is connected to the radial velocity of the fluid. In the strong field observation, we apply the method developed by Bozza (2002), which can be applied to discriminate the different types of spherically symmetric BHs and also investigate the astrophysical consequences by taking supermassive BHs in the center of nearby galaxies. We estimate the strong lensing coefficients $\bar{a}$, $\bar{b}$, and u_c/R_s (see Table 1) and the quantities of the observables θ_∞, X, and $r_{\rm mag}$ (see Table 2) for various supermassive BHs at the center of a nearby galaxy. We also evaluate these quantities for Schwarzschild, acoustic Schwarzschild, Reissner–Nordström, and acoustic charged BHs by taking the supermassive BH at the center of the galaxy with mass $M = 2.8 \times 10^6 M_\odot$ and distance $D_{\rm ol} = 8.5$ Kpc (Richstone et al. 1998; Bozza 2002) for comparison (see Table 4). It is observed in our estimation considering the same mass and distance (see Table 4) that the innermost image θ_∞ is always 4 times more than the Reissner–Nordström and Schwarzschild BHs. Also, an acoustic charged BH has a smaller image separation X and larger relative magnification $r_{\rm mag}$. The differences in their values for the

Reissner–Nordström BH are $\sim 0.44\mu$as and ~ 1.7 mag, respectively, and for the Schwarzschild BH are $\sim 0.44\mu$as and ~ 1.71 mag, respectively. It is also found that for the acoustic charged BH $\theta_\infty \in (74,\ 77)\mu$as while $X \in (0.46,\ 0.5)$ μas. This means that the outermost images for the acoustic charged BH are very closer to the innermost images and can able to be separated from the other BH images.

In addition, if the outermost relativistic image can be resolved, we could distinguish the acoustic charged BHs from a Schwarzschild BH or a Reissner–Nordström BH using the new current technology. However, the difference in X from the Schwarzschild and Reissner–Nordström BHs is not more than 0.5μas, which makes the task of discriminating the acoustic charged BHs via observation much more difficult. In Figure 3, it can be seen that the Einstein ring θ_n^E of an acoustic charged BH is greater than that of Schwarzschild and Reissner–Nordström BHs. In Table 3, we observed that the time delay between two images for the case of the acoustic charged BH (e.g., $\sim$79,502.2 minutes for NGC 4026) was significantly greater than the cases of acoustic Schwarzschild ($\sim$61,376.5 minutes), standard Reissner–Nordström ($\sim$16,900 minutes), and standard Schwarzschild ($\sim$17,378.9 minutes) BHs. It is noted that the time delay between two images for the case of the acoustic charged BH is 4 times more than the case of ordinary astrophysical BHs such as Reissner–Nordström and Schwarzschild BHs. This indicates that if one can be separated from the first and second relativistic images, the time delay between them might provide a good chance of distinguishing an acoustic charged BH from a Schwarzschild BH or a Reissner–Nordström BH. Therefore, the acoustic charged BH could be quantitatively distinguished from the standard Reissner–Nordström and standard Schwarzschild BHs.

If an acoustic charged BH can be identified, other than the standard Reissner–Nordström and standard Schwarzschild BHs, there would be a better chance of detecting the motion of the moving fluids and sound waves in a medium. With the help of gravitational lensing effects, it may be easier to detect an audible boundary of the sound waves near the acoustic BH horizon region. Indeed, the astrophysical consequences of the acoustic charged BH could be helpful in understanding the similarities and dissimilarities between sonic fluid and BH geometry. We expect that our analytical results could be used to help observe analogous BHs experiment in the future. These results could help further investigate the structure of the near-horizon geometry of ordinary astrophysical BHs.

6. Summary and Conclusions

In this work, we investigated gravitational lensing for the acoustic charged BH in curve spacetime in strong and weak field approximation. We have analyzed the effects of charged parameter Q and tuning parameter ξ on the strong deflection angle and the lensing observables θ_∞, X, $r_{\rm mag}$, Einstein ring θ_∞^E, and time delays $\Delta T_{2,1}$ in a strong lensing observation by acoustic charged BH and compared it to the cases of acoustic Schwarzschild ($Q = 0$), standard Reissner–Nordström ($\xi = 0$), and standard Schwarzschild ($\xi = 0,\ Q = 0$) BHs. We first calculate the null geodesic equation for the acoustic charged BH by the Hamilton–Jacobi action, and using this, we obtained the radius of the photon sphere r_c. We found that the photon sphere radius r_c increases with the increasing value of the tuning parameter ξ. We have numerically obtained the strong lensing coefficients $\bar{a}$, $\bar{b}$, and u_c/R_c. We found that $\bar{a}$ grows, while $\bar{b}$ grows at first, reaching its maximum value, and then decreases with the increasing magnitude of Q for the fixed value of ξ. We found that strong deflection angle α_D increases monotonically with the increasing magnitude of Q for the fixed value of ξ. It is found that the strong deflection angle α_D for the acoustic charged BH is greater than that of the standard Reissner–Nordström ($\xi = 0$) and standard Schwarzschild ($\xi = 0,\ Q = 0$) BHs. The acoustic charged BH, with the presence of tuning parameter ξ could greatly intensify the gravitational lensing effect compared to the other BHs. This result indicates that the gravitational lensing effect, due to the acoustic charged BH, is greatly enhanced compared to ordinary astrophysical BHs. Thus, the acoustic charged BHs with the presence of moving fluid and sound waves can be detected more easily and distinguished from ordinary astrophysical BHs. We numerically evaluated the strong lensing observables of the relativistic images for the supermassive BHs M87*, SgrA*, and NGC 4649 in the acoustic charged BH spacetime background. We have seen that for the fixed value of ξ, angular position θ_∞ decreases while angular separation X increases with the increasing magnitude of Q. In the case where $\xi = 0$ and $0 \leqslant |Q| \leqslant 0.5$, $\theta_\infty \in (15.22,\ 19.783)\mu$as for M87*, $\theta_\infty \in (20.24,\ 26.303)$ μas for SgrA*, and $\theta_\infty \in (11.28,\ 14.662)$ μas for NGC 4649; for the case where $\xi = 4$ and $0 \leqslant |Q| \leqslant 0.5$, $\theta_\infty \in (65.49,\ 69.865)\mu$as for M87*, $\theta_\infty \in (87.08,\ 92.891)\mu$as for SgrA*, and $\theta_\infty \in (48.54,\ 51.781)$ μas for NGC 4649, and the case where $\xi = 5$ and $0 \leqslant |Q| \leqslant 0.5$, $\theta_\infty \in (86.56,\ 90.497)\mu$as for M87*, $\theta_\infty \in (115.092,\ 120.323)\mu$as for SgrA*, and $\theta_\infty \in (64.15,\ 67.073)\mu$as for NGC 4649.

On the other hand, the angular separation $X \in (0.024,\ 0.107)$ μas for M87*, $X \in (0.032,\ 0.142)\mu$as for SgrA*, $X \in (0.018,\ 0.0791)\mu$as for NGC 4649 for the case when $\xi = 0$ and $0 \leqslant |Q| \leqslant 0.5$; $X \in (0.76,\ 0.959)\mu$as for M87*, $X \in (1.01,\ 1.28)\mu$as for SgrA* $X \in (0.56,\ 0.711)\mu$as for NGC 4649 and the case when $\xi = 5$ and $0 \leqslant |Q| \leqslant 0.5$ and $X \in (0.54,\ 0.635)\mu$as for M87*, $X \in (0.72,\ 0.844)\mu$as for SgrA*, $X \in (0.40,\ 0.471)\mu$as for NGC 4649 for the case when $\xi = 0$ and $0 \leqslant |Q| \leqslant 0.5$.

The magnification of the relativistic images $r_{\rm mag}$ decreases with the increasing magnitude of Q for the fixed value of $\xi(= 0,\ 4,\ 5)$ and for $0 \leqslant |Q| \leqslant 0.5$, $r_{\rm mag} \in (4.82,\ 6.822)$, $r_{\rm mag} \in (3.95,\ 4.302)$ for $r_{\rm mag} \in (3.95,\ 4.302)$, and $r_{\rm mag} \in (4.91,\ 5.12)$ order of magnitude, respectively, for the cases of $\xi = 0$, $\xi = 4$, and $\xi = 5$. By considering the supermassive BHs SgrA* and M87*, the outermost Einstein ring θ_n^E for the cases of $\xi = 0$ and $\xi = 4$ are presented in Figure 3. It is found that the radius of the Einstein ring θ_n^E decreases with the increasing magnitude of Q and the Einstein ring θ_n^E of an acoustic charged BH is greater than that of the acoustic Schwarzschild ($Q = 0$) BH, which is greater than the standard Schwarzschild ($\xi = 0,\ Q = 0$) BH. We have also evaluated the time delays $\Delta T_{2,1}$ between first- and second-order relativistic images for various supermassive BHs in the background of the standard Schwarzschild ($\xi = 0,\ Q = 0$), acoustic Schwarzschild ($\xi = 4,\ Q = 0$), and acoustic charged ($\xi = 5,\ Q = 0.05$) BHs. We observed that the time delay $\Delta T_{2,1}$ for the case of the acoustic charged ($\xi = 5,\ Q = 0.05$) BH (e.g.,$\sim$79,502.2 minutes for NGC 4026) was significantly greater than in the case of the acoustic Schwarzschild ($\xi = 4,\ Q = 0$) and standard Schwarzschild ($\xi = 0,\ Q = 0$) BHs. Furthermore, we have discussed the weak gravitational lensing by the acoustic charged BH and compared it to the

Table 4
Estimation of Observables by Taking the Supermassive BH Having Mass $M = 2.8 \times 10^6 M_\odot$ and Distance $D_{ol} = 8.5$ Kpc in the Context of Standard Schwarzschild, Acoustic Schwarzschild, Reissner–Nordström, and Acoustic Charged BH Spacetimes

	Schwarzschild	Acoustic Schwarzschild	Reissner–Nordström			Acoustic Charged BH		
			$Q = 0.1$	$Q = 0.3$	$Q = 0.4$	$Q = 0.1$	$Q = 0.3$	$Q = 0.4$
θ_∞ (μas)	16.8427	59.4828	16.7295	15.7488	14.7352	76.9527	75.9077	74.9625
X (μas)	0.02108	0.649386	0.0216	0.02749	0.03789	0.46499	0.49779	0.50838
r_{mag}	6.82188	4.30153	6.79092	6.48573	6.07469	5.11286	5.02951	4.99391
u_c/R_s	2.59808	9.17557	2.58062	2.42935	2.27299	11.8704	11.7092	11.5634
$\bar{a}$	1	1.58592	1.00456	1.05183	1.123	1.33426	1.35637	1.36604
$\bar{b}$	−0.4002	−0.88108	−0.3993	−0.39651	−0.4136	−0.53343	−0.53542	−0.5382

standard Schwarzschild ($\xi = 0$, $Q = 0$) and acoustic Schwarzschild ($\xi = 4$, $Q = 0$) BHs. We have seen that for the fixed value of ξ, the weak deflection angle decreases with the increasing magnitude of Q as well as the impact parameter b. Therefore, our results suggest how the acoustic charged BHs are detected by astronomical observations and the results of the acoustic charged BH are a generalization of the previous investigation of acoustic Schwarzschild ($Q = 0$), standard Reissner–Nordström ($\xi = 0$), and standard Schwarzschild ($\xi = 0$, $Q = 0$) BHs.

Appendix

Weak deflection angle of a massive particle, source and receiver located at finite distance region: In the Section 5, we obtain the weak deflection angle by warner's method for the cases where the source and receiver are located at the infinite-distance region. In this Appendix, we derive the weak deflection angle from the Gauss Bonet-Theorem in the cases where the receiver and source are located at finite distance regions. Recently, Qiao & Zhou (2021) derived the weak deflection angle for the finite distance region for the acoustic Schwarzchild BH. To calculate the weak deflection angle for the finite distance region, Qiao & Zhou (2021) considered the method proposed by Ishihara et al. (2017, 2016). We apply this method to the case of acoustic charged BH.

For the spacetime (42), the geodesic curvature of the particle ray η_g can be obtained as (Ono et al. 2017)

$$\begin{aligned}\kappa_g &= \frac{1}{2\sqrt{\gamma_{\phi\phi}}}\frac{\partial \gamma_{rr}}{\partial \phi} = \frac{F(r)}{r} - \frac{1}{2}\frac{\partial F(r)}{\partial r} \\ &= \frac{1}{r} - \frac{3M(1+\xi^2)}{r^2} + \frac{2(8M^2\xi + 8Q^2 + Q^2\xi)}{r^3} \\ &- \frac{20M\xi(M^2+Q^2)}{r^4} \\ &+ \frac{6Q^2\xi(6M^2+Q^2)}{r^5} + \frac{21MQ^4\xi}{r^6} + \frac{Q^6\xi}{r^7}.\end{aligned} \tag{A1}$$

With the help of the Gaussian curvature in Equation (46), surface area in Equation (47), geodesic curvature in Equation (A1) and using the relation $r(\gamma) = r(\phi) \approx \frac{b}{\sin(\phi)}$, the deflection angle of massive particles in weak field limit for the finite distance region, can

be calculated in the following (Qiao & Zhou 2021)

$$\sigma_D|F.D = \psi_S - \psi_O + \phi_{OS} = -\int_{\phi_S}^{\phi_o} d\phi \int_{r(\gamma)}^{\infty} K\frac{r}{[F(r)]^{\frac{3}{2}}}dr$$
$$\approx -\int_{\phi_S}^{\phi_o} d\phi \int_{\frac{b}{\sin\phi}}^{\infty} K\frac{r}{[F(r)]^{\frac{3}{2}}}dr$$
$$= -\int_{\phi_S}^{\phi_o} d\phi \int_{\frac{b}{\sin\phi}}^{\infty} K\frac{r}{[F(r)]^{\frac{3}{2}}}dr$$
$$= -\int_{\phi_S}^{\phi_o} d\phi \int_{\frac{b}{\sin\phi}}^{\infty} \left[\frac{3Q^2(1+\xi)}{r^3} + \frac{M\{6Q^2(\xi^2-6\xi+1) - 2r^2(1+\xi)\}}{r^4}\right.$$
$$+ \frac{M^2\{15Q^2(\xi^3-5\xi^2+3\xi+1) - 3r^2(\xi^2-6\xi+1)\}}{r^5}$$
$$+ \frac{3M^2\{5Q^2(5\xi^4-28\xi63+30\xi^2+4\xi+5) - 4r^2(\xi^3-5\xi^2+3\xi+1)\}}{2r^6}$$
$$\left. + \mathcal{O}\left(\left(\frac{M}{r}\right)^4, \left(\frac{Q}{r}\right)^4\right)\right]dr$$
$$= -\int_{\phi_S}^{\phi_o} \left[\frac{3Q^2(1+\xi)\sin^2\phi}{2b^2} + \frac{M\{2Q^2(\xi^2-6\xi+1)\sin^3\phi - 2b^2(1+\xi)\sin\phi\}}{b^3}\right.$$
$$+ \frac{M^2\{15Q^2(\xi^3-5\xi^2+3\xi+1)\sin^4\phi - 6b^2(\xi^2-6\xi+1)\sin^2\phi\}}{4b^4}$$
$$+ \frac{3M^3Q^2(5\xi^4-28\xi^3+30\xi^2+4\xi+5)\sin^5\phi}{2b^5}$$
$$\left. - \frac{2M^3(\xi^3-5\xi^2+3\xi+1)\sin^3\phi}{b^3} + \mathcal{O}\left(\frac{M^4}{b^6}, \frac{Q^4}{b^6}\right)\right]d\phi$$
$$= \frac{2(1+\xi)M}{b}[\cos(\phi_s) - \cos(\phi_o)] - \left\{\frac{3Q^2(\xi+1)}{4b^2}\right.$$
$$\left. - \frac{3M^2(\xi^2-6\xi+1)}{4b^2}\right\}$$
$$[\phi_{\rm os} + \cos(\phi_s)\sin(\phi_s) - \cos(\phi_o)\sin(\phi_o)]$$
$$- \{\frac{2MQ^2(\xi^2-6\xi+1)}{3b^3} - \frac{2M^3}{3b^3}(\xi^3-5\xi^2+3\xi+1)\}$$
$$[\cos\phi_s(2+\sin^2\phi_s) - \cos\phi_o(2+\sin^2\phi_o)]$$
$$- \frac{15M^2Q^2(\xi^3-5\xi^2+3\xi+1)}{128b^4}\{12\phi_{\rm os} - 8[\sin(2\phi_s) - \sin(2\phi_o)]$$
$$+ [\sin(4\phi_s) - \sin(4\phi_o)]\}$$
$$- \frac{3M^3Q^2(5\xi^4-28\xi^3+30\xi^2+4\xi+5)\sin^5\phi}{480b^5}$$
$$\{150[\cos(\phi_s) - \cos(\phi_o)]$$
$$- 25[\cos(3\phi_s) - \cos(3\phi_o)] + 3[\cos(5\phi_s) - \cos(5\phi_o)]\}$$
$$+ \mathcal{O}\left(\frac{M^4}{b^6}, \frac{Q^4}{b^6}\right) \tag{A2}$$

To find the azimuthal angle ϕ_S and ϕ_O , we use the leading order approximation solution of particle orbit

$$r(\gamma) \approx \frac{b}{\sin\phi} \Rightarrow \sin\phi \approx \frac{b}{r} \approx bu. \tag{A3}$$

From the weak lensing diagram, (Qiao & Zhou 2021, see Figure 5), azimuthal angles satisfies $\phi_S < \frac{\pi}{2}$ and $\phi_O > \frac{\pi}{2}$. The trigonometric functions of azimuthal angles become

$$\cos(\phi_s) = \sqrt{1 - b^2u_s^2}\,; \cos(\phi_o) = -\sqrt{1 - b^2u_o^2}\,. \tag{A4}$$

Finally, the deflection angle in the weak field limit for the finite-distance region can be obtained as

$$\sigma_D|F.D = \frac{2(\xi+1)M}{b}[\sqrt{1-b^2u_s^2}+\sqrt{1-b^2u_o^2}]$$
$$-\{\frac{3Q^2(1+\xi)}{4b^2}-\frac{3(\xi^2-6\xi+1)M^2}{4b^2}\}$$
$$[\pi-\arcsin(bu_s)-\arcsin(bu_o)$$
$$+bu_s\sqrt{1-b^2u_s^2}+bu_o\sqrt{1-b^2u_o^2}]$$
$$-\{\frac{2MQ^2(\xi^2-6\xi+1)}{3b^3}-\frac{2M^3(\xi^3-5\xi^2+3\xi+1)}{3b^3}\}$$
$$[(2+b^2u_s^2)\sqrt{1-b^2u_s^2}+(2+b^2u_s^2)\sqrt{1-b^2u_s^2}]$$
$$-\frac{15M^2Q^2(\xi^3-5\xi^2+3\xi+1)}{32b^4}\{3[\pi-\arcsin(bu_s)-\arcsin(bu_o)]$$
$$-4[bu_s\sqrt{1-b^2u_s^2}+bu_o\sqrt{1-b^2u_o^2}]$$
$$+[bu_s(1-b^2u_s^2)^{\frac{3}{2}}+bu_o(1-b^2u_o^2)^{\frac{3}{2}}]$$
$$-[b^3u_s^3\sqrt{1-b^2u_s^2}+b^3u_o^3\sqrt{1-b^2u_o^2}]\}$$
$$-\frac{3M^3Q^2(5\xi^4-28\xi^3+30\xi^2+4\xi+5)\sin^5\phi}{480b^5}$$
$$\{150[\sqrt{1-b^2u_s^2}+\sqrt{1-b^2u_o^2}]$$
$$-25[(1-b^2u_s^2)^{\frac{3}{2}}+(1-b^2u_o^2)^{\frac{3}{2}}]$$
$$+3[(1-b^2u_s^2)^{\frac{5}{2}}+(1-b^2u_o^2)^{\frac{5}{2}}]$$
$$+75[b^2u_s^2\sqrt{1-b^2u_s^2}+b^2u_o^2\sqrt{1-b^2u_o^2}]$$
$$+30[b^2u_s^2(1-b^2u_s^2)^{\frac{3}{2}}+b^2u_o^2(1-b^2u_o^2)^{\frac{3}{2}}]$$
$$+15[b^4u_s^4\sqrt{1-b^2u_s^2}+b^4u_o^4\sqrt{1-b^2u_o^2}]\}+\mathcal{O}\left(\frac{M^4}{b^6},\frac{Q^4}{b^6}\right). \quad \text{(A5)}$$

This is the finite-distance deflection angle in the weak field limit approximation by acoustic charged black hole where the receiver and source are located at a finite distance region from the lens (BH).

For the infinite distances, we have $u_S \to 0$ and $u_O \to 0$,So the deflection angle by acoustic charged black hole becomes

$$\sigma_D \to -\frac{3\pi Q^2(1+\xi)}{4b^2}$$
$$-\frac{M\{8Q^2(\xi^2-6\xi+1)-12b^2(1+\xi)\}}{3b^3}$$
$$-\frac{M^2\pi\{45Q^2(\xi^3-5\xi^2+3\xi+1)-24b^2(\xi^2-6\xi+1)\}}{32b^4}$$
$$-\frac{8M^3Q^2(5\xi^4-28\xi63+30\xi^2+4\xi+5)}{5b^5}$$
$$+\frac{8M^3(\xi^3-5\xi^2+3\xi+1)}{3b^3}+\mathcal{O}\left(\frac{M^4}{b^6},\frac{Q^4}{b^6}\right), \quad \text{(A6)}$$

which is basically the infinite-distance deflection angle $\sigma_D|\infty$ obtained in Equation (48).

ORCID iDs

Niyaz Uddin Molla https://orcid.org/0000-0003-2460-3634

References

Abbott, T. D., et al. 2016, PhRvX, 6, 041014
Akiyama, K., Alberdi, A., Alef, W., et al. 2019a, ApJL, 875, L1
Akiyama, K., Alberdi, A., Alef, W., et al. 2019b, ApJL, 875, L4
Anacleto, M. A., Brito, F. A., & Passos, E. 2011, PhLB, 694, 149
Anacleto, M. A., Brito, F. A., & Passos, E. 2012, PhRvD, 85, 025013
Arakida, H. 2018, GReGr, 50, 48
Bartelmann, M., & Schneider, P. 2001, PhR, 340, 291
Bellagamba, F., Sereno, M., Roncarelli, M., et al. 2019, MNRAS, 484, 1598
Benone, C. L., Crispino, L. C. B., Herdeiro, C., & Radu, E. 2015, PhRvD, 91, 104038
Bisnovatyi-Kogan, G. S., & Tsupko, O. Y. 2008, GrCo, 14, 226
Bozza, V. 2002, PhRvD, 66, 103001
Bozza, V. 2003, PhRvD, 67, 103006
Bozza, V., Capozziello, S., Iovane, G., & Scarpetta, G. 2001, GReGr, 33, 1535
Bozza, V., De Luca, F., Scarpetta, G., & Sereno, M. 2005, PhRvD, 72, 083003
Bozza, V., & Mancini, L. 2004, GReGr, 36, 435
Briet, J., & Hobill, D. 2008, arXiv:0801.3859
Brouwer, M. M., Demchenko, V., Harnois-Deraps, J., et al. 2018, MNRAS, 481, 5189

Cao, S., Covone, G., & Zhu, Z.-H. 2012, ApJ, 755, 31
Cardoso, V., Lemos, J. P. S., & Yoshida, S. 2004, PhRvD, 70, 124032
Cardoso, V., Miranda, A. S., Berti, E., Witek, H., & Zanchin, V. T. 2009, PhRvD, 79, 064016
Chen, S., & Jing, J. 2009, PhRvD, 80, 024036
Claudel, C.-M., Virbhadra, K. S., & Ellis, G. F. R. 2001, JMP, 42, 818
Crisnejo, G., & Gallo, E. 2018, PhRvD, 97, 124016
Crisnejo, G., Gallo, E., & Jusufi, K. 2019a, PhRvD, 100, 104045
Crisnejo, G., Gallo, E., & Rogers, A. 2019b, PhRvD, 99, 124001
Darwin, C. G. 1959, RSPSA, 249, 180
de Leon, K., & Vega, I. 2019, PhRvD, 99, 124007
Einstein, A. 1936, Sci, 84, 506
Eskin, G. 2019, arXiv:1906.06038
Fischer, U. R., & Visser, M. 2002, PhRvL, 88, 110201
Fischer, U. R., & Visser, M. 2003, AnPhy, 304, 22
Ge, X.-H., Nakahara, M., Sin, S.-J., Tian, Y., & Wu, S.-F. 2019, PhRvD, 99, 104047
Ge, X.-H., & Sin, S.-J. 2010, JHEP, 06, 087
Ge, X.-H., Sun, J.-R., Tian, Y., Wu, X.-N., & Zhang, Y.-L. 2015, PhRvD, 92, 084052
Ge, X. H., Wu, S. F., Wang, Y., Yang, G. H., & Shen, Y. G. 2012, IJMPD, 21, 1250038
Ghosh, S. G., Kumar, R., & Islam, S. U. 2021, JCAP, 03, 056
Gibbons, G. W., & Werner, M. C. 2008, CQGra, 25, 235009
Gillessen, S., Plewa, P. M., Eisenhauer, F., et al. 2017, ApJ, 837, 30
Goulart, P. 2018, CQGra, 35, 025012
Guerrero, M., Mora-Perez, G., Olmo, G. J., Orazi, E., & Rubiera-Garcia, D. 2020, JCAP, 2020, 058
Gueth, F., & Guilloteau, S. 1999, A&A, 343, 571
Guo, H., Liu, H., Kuang, X.-M., & Wang, B. 2020, PhRvD, 102, 124019
Guzik, J., Jain, B., & Takada, M. 2010, PhRvD, 81, 023503
Haroon, S., Jamil, M., Jusufi, K., Lin, K., & Mann, R. B. 2019, PhRvD, 99, 044015
He, H.-J., & Zhang, Z. 2017, JCAP, 08, 036
Hod, S. 2009, PhRvD, 80, 064004
Hsieh, T., Lee, D.-S., & Lin, C.-Y. 2021, PhRvD, 104, 104013
Huterer, D., & Shafer, D. L. 2018, RPPh, 81, 016901
Ishihara, A., Suzuki, Y., Ono, T., & Asada, H. 2017, PhRvD, 95, 044017
Ishihara, A., Suzuki, Y., Ono, T., Kitamura, T., & Asada, H. 2016, PhRvD, 94, 084015
Islam, S. U., & Ghosh, S. G. 2021, PhRvD, 103, 124052
Islam, S. U., Ghosh, S. G., & Maharaj, S. D. 2022, arXiv:2203.00957
Islam, S. U., Kumar, J., & Ghosh, S. G. 2021, JCAP, 10, 013
Islam, S. U., Kumar, R., & Ghosh, S. G. 2020, JCAP, 09, 030
Javed, W., Abbas, J., & Övgün, A. 2019a, EPJC, 79, 694
Javed, W., Babar, R., & Övgün, A. 2019b, PhRvD, 99, 084012
Javed, W., Khadim, M. B., Abbas, J., & Övgün, A. 2020a, EPJP, 135, 1
Javed, W., Khadim, M. B., & Övgün, A. 2020b, EPJP, 135, 595
Javed, W., Khadim, M. B., Övgün, A., & Abbas, J. 2020c, EPJP, 135, 314
Jha, S. K., & Rahaman, A. 2022, arXiv:2205.06052
Jung, S., & Shin, C. S. 2019, PhRvL, 122, 041103
Jusufi, K. 2016, Ap&SS, 361, 24
Jusufi, K., & Ovgun, A. 2018, PhRvD, 97, 024042
Jusufi, K., Övgün, A., Banerjee, A., & Sakallı, t. 2019, EPJP, 134, 428
Jusufi, K., Ovgun, A., Saavedra, J., Vasquez, Y., & Gonzalez, P. A. 2018, PhRvD, 97, 124024
Jusufi, K., Sakallı, I., & Övgün, A. 2017, PhRvD, 96, 024040
Kaiser, N., & Squires, G. 1993, ApJ, 404, 441
Kormendy, J., & Ho, L. C. 2013, ARA&A, 51, 511
Kumar, J., Islam, S. U., & Ghosh, S. G. 2022a, EPJC, 82, 443
Kumar, J., Islam, S. U., & Ghosh, S. G. 2022b, ApJ, 938, 104
Kumar, R., Ghosh, S. G., & Wang, A. 2019, PhRvD, 100, 124024
Kumar, R., Ghosh, S. G., & Wang, A. 2020a, PhRvD, 101, 104001
Kumar, R., Islam, S. U., & Ghosh, S. G. 2020b, EPJC, 80, 1128
Kumar, R., Singh, B. P., & Ghosh, S. G. 2020c, AnPhy, 420, 168252
Li, Z., & Jia, J. 2020, EPJC, 80, 157
Li, Z., & Ovgun, A. 2020, PhRvD, 101, 024040
Li, Z., & Zhou, T. 2020, PhRvD, 101, 044043
Liebes, S. 1964, PhRv, 133, B835
Lima, C. A. U., Brito, F., Hoyos, J. A., & Vanzella, D. A. T. 2019, NatCo, 10, 3030
Ling, R., Guo, H., Liu, H., Kuang, X.-M., & Wang, B. 2021, PhRvD, 104, 104003
Man, J., & Cheng, H. 2014, JCAP, 11, 025
Massey, R., Kitching, T., & Richard, J. 2010, RPPh, 73, 086901
Mellier, Y. 1999, ARA&A, 37, 127
Meneghetti, M., Bartelmann, M., Dahle, H., & Limousin, M. 2013, SSRv, 177, 31
Molla, N. U., & Debnath, U. 2022, IJGMM, 19, 2250183
Mustafa, G., Atamurotov, F., Hussain, I., Shaymatov, S., & Övgün, A. 2022, ChPhC, 46, 125107
Ohanian, H. C. 1987, AmJPh, 55, 428
Ono, T., & Asada, H. 2019, Univ, 5, 218
Ono, T., Ishihara, A., & Asada, H. 2017, PhRvD, 96, 104037
Ono, T., Ishihara, A., & Asada, H. 2018, PhRvD, 98, 044047
Ono, T., Ishihara, A., & Asada, H. 2019, PhRvD, 99, 124030
Ovgun, A., Gyulchev, G., & Jusufi, K. 2019, AnPhy, 406, 152
Pang, X., & Jia, J. 2019, CQGra, 36, 065012
Petters, A. O., Levine, H., & Wambsganss, J. 2001, Singularity Theory and Gravitational Lensing (Boston, MA: Birkhäuser)
Qiao, C.-K., & Zhou, M. 2021, arXiv:2109.05828
Qiao, C.-K., & Zhou, M. 2022, arXiv:2212.13311
Refsdal, S. 1964a, MNRAS, 128, 295
Refsdal, S. 1964b, MNRAS, 128, 307
Richstone, D., Ajhar, E., Bender, R., et al. 1998, Natur, 385, A14
Sakalli, I., & Ovgun, A. 2017, EPL, 118, 60006
Sarkar, K., & Bhadra, A. 2006, CQGra, 23, 6101
Schmidt, F. 2008, PhRvD, 78, 043002
Schneider, P., Ehlers, J., & Falco, E. 1992, Gravitational Lenses (Berlin: Springer), doi:10.1007/978-3-662-03758-4
Sereno, M. 2003, MNRAS, 344, 942
Sereno, M. 2004, PhRvD, 69, 023002
Shaikh, R., Banerjee, P., Paul, S., & Sarkar, T. 2019, PhRvD, 99, 104040
Stefanov, I. Z., Yazadjiev, S. S., & Gyulchev, G. G. 2010, PhRvL, 104, 251103
Unruh, W. G. 1981, PhRvL, 46, 1351
Vanderveld, R. A., Mortonson, M. J., Hu, W., & Eifler, T. 2012, PhRvD, 85, 103518
Vieira, H. S., & Kokkotas, K. D. 2021, PhRvD, 104, 024035
Virbhadra, K. S., & Ellis, G. F. R. 2000, PhRvD, 62, 084003
Virbhadra, K. S., & Ellis, G. F. R. 2002, PhRvD, 65, 103004
Virbhadra, K. S., & Keeton, C. R. 2008, PhRvD, 77, 124014
Wang, Y., Stebbins, A., & Turner, E. L. 1996, PhRvL, 77, 2875
Werner, M. C. 2012, GReGr, 44, 3047
Will, C. M. 2015, CQGra, 32, 124001
Wittman, D. M., Tyson, J. A., Kirkman, D., Dell'Antonio, I., & Bernstein, G. 2000, Natur, 405, 143
Zhao, S.-S., & Xie, Y. 2016, JCAP, 07, 007